MRI and histologic studies on early markers of Alzheimer's disease

Duijn, S. van

Chapter 5

Detection of cortical changes in Alzheimer's disease patients at ultra-high field MRI

R.J.A. Nabuurs, MD PhD #1, S van Rooden, MSc #1, S van Duijn, MSc 2, M.J. Versluis, PhD 1, B.J. Emmer, MD, PhD 1, M.K. Liem, MD, PhD 1, J.R. Milles, PhD 3, A.G. Webb, PhD 1, M.P. Frosch, MD, PhD 4, S.G. van Duinen, MD, PhD 2, R Natté, MD, PhD 2, J van der Grond, PhD 1, L van der Weerd, PhD 1,5, M.A. van Buchem, MD, PhD 1

Authors have contributed to this work equally.
1. Department of Radiology, Leiden University Medical Centre, Albinusdreef 2, 2333 ZA, Leiden, Netherlands
2. Department of Pathology, Leiden University Medical Centre, Albinusdreef 2, 2333 ZA, Leiden, Netherlands
3. Division of Image Processing (LKEB), Department of Radiology, Leiden University Medical Centre, Albinusdreef 2, 2333 ZA, Leiden, Netherlands
4. C.S. Kubik Laboratory for Neuropathology, Massachusetts General Hospital and Harvard Medical School, 55 Fruit Street,
Boston, MA 02114, USA
5. Department of Human Genetics, Leiden University Medical Centre, 2333 ZA, Albinusdreef 2, Leiden, Netherlands

Abstract

Non-invasive methods to detect Alzheimer's disease (AD) in vivo at an early stage are important to increase our still-incomplete understanding of the pathophysiology of the disease. In this study we assessed whether differences in cortical appearance could be observed in AD patients using 7T magnetic resonance imaging in vivo and to assess the nature of these changes by a histological-radiological correlation ex vivo. In vivo regional cortical differences between probable AD patients (n=14, mean age 76.4 years (range: 68 - 86), 9 males) and healthy control subjects (n=15, mean age 75.1 years (range: 69 – 80), 10 males), visible on 7T susceptibility-weighted images, were analyzed after defining a novel scoring method based on the cortical appearance. In addition, postmortem magnetic resonance imaging of confirmed AD cases (n=6) was performed to assess the histological correlates of the changes observed in vivo in AD patients. A chi-square test showed that diffuse hypointense bands were frequently found in the cortex of the frontal lobes of AD patients (57%), but not in controls, $p = 0.001$. Histologic correlation revealed that the pattern of the susceptibility-weighted contrast in the cortex of AD patients does not primarily co-localize with amyloid plaques or neurofibrillary tangles, but with microglia- and myelin-associated iron accumulation and with an altered myelin cytoarchitecture. Our observation of disturbed iron accumulation and myelin architecture in AD has important implications for the understanding of the pathophysiological mechanisms underlying this disease, and also for in vivo diagnosis of AD.

Keywords: Alzheimer's disease, cortex, beta-amyloid, magnetic resonance imaging, iron.

Abbreviations: amyloid-beta (Aβ), diaminobenzidine-tetrahydrochloride (DAB), echo time (TE), electron microscopy (EM), gray matter (GM), Mini Mental State Examination (MMSE), National Institute of Neurological and Communicative Disorders and Stroke and Alzheimer's disease and Related Disorders Association (NINCDS-ADRDA), paired helical filament-tau (AT8), protolipid-protein (PLP), repetition time (TR), susceptibility-weighted (SW), white matter (WM).

Introduction

For the definitive diagnosis of Alzheimer's disease (AD) histological post-mortem detection of amyloid plaques and neurofibrillary tangles is required. During life, only a probable diagnosis can be made that is based primarily on clinical signs and symptoms (Montine et al., 2012). However, recently it has been proposed to use biomarkers based on CSF analysis, structural MRI and amyloid imaging using PET, as supporting diagnostic criteria in research settings (Jack, Jr. et al., 2010).

Over the past few years, the feasibility of detecting the histological hallmarks of AD using MRI has been explored by many research groups. In general these efforts have focused on detecting individual amyloid plaques: increased iron accumulation around amyloid plaques induces a magnetic susceptibility effect, which is visible as hypointense foci on T2*-weighted or susceptibility-weighted (SW) MRI in the cerebral cortex of transgenic AD mouse models and in human post-mortem brain slices (van Rooden et al., 2009; Meadowcroft et al., 2009; Chamberlain et al., 2011). However, these findings have not yet been convincingly replicated in vivo in patients, and it is doubtful whether detecting individual amyloid plaques with MRI will be possible in a clinical setting given the required high anatomical resolution, limited scanning time, and physiological motion of the patient. Furthermore, the central role of amyloid in the pathophysiology of AD remains a topic of debate. Although amyloid is still considered to be a hallmark as well as an initiating factor in the progression of the disease, there is increasing evidence that other primary or interacting causes, including changes in iron metabolism, may exist (Karran et al., 2011; Fjell and Walhovd, 2012).

Recent advances in human MRI systems operating at an ultra-high magnetic field strength (7 Tesla and higher) show that the increased sensitivity to susceptibility effects generates iron-based contrasts in the human brain that have not been observed at lower fields (Fukunaga et al., 2010). The aim of our study was to establish whether 7T MRI allows in vivo detection of differences in the cerebral cortex between probable Alzheimer's disease patients and healthy age-matched controls. Having observed a difference, we then determined the histological substrate of the changes by comparing MRI to light- and electron microscopy (EM) of human post-mortem material of Alzheimer's disease patients and controls.

Table 1: Characteristics of patients and controls and scoring results of *in vivo* the SW imaging study

	Alzheimer's disease (n = 14)	Controls (n = 15)	p-value
Characteristics:			
Male / female	9/5	10/5	0.893
Mean age (range, yrs)	76.4 (68 – 86)	75.1 (69 – 80)	0.497
MMSE (range)	22.5 (19 - 26)	29.2 (27 – 30)	0.000
Presence of homogeneous layer			
Superior frontal lobe	12/14 (85.7%)	15/15 (100%)	0.224
Middle and inferior frontal lobe	5/14 (35.7%)	9/15 (60%)	0.006
Presence of two layers			
Superior frontal lobe	2/14 (14.3%)	5/15 (33.3%)	0.390
Middle and inferior frontal lobe	10/14 (71.4%)	13/15 (86.6%)	0.390
Presence of three layers			
Superior frontal lobe	0/14 (0%)	2/15 (13.3%)	0.483
Middle and inferior frontal lobe	3/14 (21.4%)	3/15 (20%)	1.000
Presence of diffuse band			
Superior frontal lobe	2/14 (14.3%)	0/15 (0%)	0.224
Middle and inferior frontal lobe	8/14 (57.1%)	0/15 (0%)	0.001
Hypo-intense foci			
Superior frontal lobe	0/14 (0%)	0/15 (0%)	-
Middle and inferior frontal lobe	0/14 (0%)	0/15 (0%)	-

Materials and Methods

A. In vivo MRI study:

Participants

This study was approved by the institutional review board. In all cases, informed consent was obtained according to the declaration of Helsinki. Fourteen probable AD patients (mean age 76.4 years (range: 68 - 86), 9 males) and fifteen control subjects (mean age 75.1 years (range: 69 – 80), 10 males) were included (table 1). Alzheimer's disease patients were recruited from the memory outpatient clinic of our institution. Memory outpatient clinic patients were referred to the hospital by their general practitioner or a medical specialist. Prior to the 7T MRI study these patients all underwent a routine clinical protocol, comprising a whole brain MRI (performed on a clinical 3 Tesla platform), a battery of neuropsychological tests, and a general medical and neurological examination performed by a neurologist, psychiatrist or internist-geriatrician. The diagnosis was made in a multidisciplinary consensus meeting using the National Institute of Neurological and Communicative Disorders and Stroke and AD and Related Disorders Association (NINCDS-ADRDA) criteria for diagnosing probable AD (McKhann et al., 1984). Participants with the diagnosis 'probable Alzheimer's disease', who were capable of giving informed consent and who had a Mini Mental State Examination (MMSE) of ≥19 were selected for inclusion in the 7T study, either retrospectively within one year after attending the memory clinic, or prospectively. Healthy control subjects were recruited by focused advertisements. Subjects between 69 and 80 years of age, who were living independently and had an MMSE of ≥25 and a Geriatric Depression Scale (GDS) of ≤4 were selected for inclusion. Control subjects with the following diseases were excluded: stroke, Parkinson's disease, diabetes mellitus, rheumatoid arthritis, polymyalgia rheumatica, cancer, heart failure, and chronic obstructive pulmonary disease.

MRI data acquisition

Our study was performed on a human whole-body MRI system operating at a magnetic field strength of 7 Tesla (Philips Healthcare, Best, The Netherlands) using a quadrature transmit and 16-channel receive head coil (Nova Medical, Wilmington, MA, USA). Alzheimer's disease-related pathology spreads throughout almost the entire brain, but macroscopically

Table 2: Post-mortem subject characteristics and SW imaging analysis.

Subject characteristics						9.4 T SW imaging analysis			
No.	Age / Sex	Diagnose	Cause(s) of death	Braak	Amyloid	Homogenous with cortical layers	Diffuse band	Hypo-intense foci	Clouds
1	83 / F	Control	Arrhythmia	II	0	Yes	-	-	-
2	93 / F	Control	Acute death	I	A	Yes	-	-	-
3	89 / F	Control	Myocardial infarct / Pneumonia	III	A	No	+	+	+
4	77 / M	AD	Cachexia / dehydration by advanced dementia syndrome	VI	C	No	+	+	-
5	85 / F	AD	Aspiration pneunomia by advanced dementia syndrome	IV	C	No	+	-	+
6	87 / F	AD	Respiratory tract infection / cerebrovascular accident	VI	C	No	+	-	+
7	87 / M	AD	Cachexia / dehydration by advanced dementia syndrome	V	C	No	+	+	-
8	87 / F	AD	Sepsis	V	C	No	-	-	+
9	88 / F	AD	Unknown	IV	C	No	+	-	+

typically involves the fronto-temporal association cortices (Duyckaerts et al., 2009; Bartzokis, 2011; Alves et al., 2012). Participants were scanned using a 2D flow-compensated axial T2*-weighted gradient-echo sequence which included the frontal lobe for detection of Alzheimer's disease pathology with a total imaging duration of 10 minutes. Imaging parameters were: repetition time (TR)/echo time (TE) 794/25 ms, flip angle 45°, slice thickness 1.0 mm with a 0.1 mm interslice gap, 20 slices, 240 x 180 x 22 mm field of view, 1024x768 matrix size – resulting in an in-plane spatial resolution of 0.24 x 0.24 mm2. The bandwidth per pixel was 46 Hz, corresponding to a readout length of approximately 22 ms. Frequency and phase encoding directions were along the anterior-posterior and right-left axes, respectively. This sequence is very sensitive to image artifacts arising from resonance frequency fluctuations within the brain caused by slight patient movements, even in areas significantly away from the head, and so a navigator echo was included to correct for these artifacts.(Versluis et al., 2010) Shimming up to third order was performed using an image based shimming approach (Schar et al., 2004). Phase images were unwrapped by high-pass filtering with a 92x92 kernel size. SW images were constructed by applying four phase mask multiplications (Haacke et al., 2004).

Whole brain imaging at this high spatial resolution (0.24 x 0.24 x 1 mm3) however would result in an impractically long imaging duration, particularly for Alzheimer's disease patients (Versluis et al., 2010). Since susceptibility artifacts induced by the temporal bone hampered the imaging of the temporal lobe, the final imaging volume focused on the frontal lobe, which is less prone to atrophy than the temporal lobe, but is known to accumulate high amyloid loads (Rowe and Villemagne, 2011), to have a lower metabolic rate (Langbaum et al., 2009), and to have an altered

resting state network connectivity in Alzheimer's disease(Rombouts et al., 2005).

Image analysis

Based on previous 7T MRI studies of the human cortex in post-mortem brain specimens of Alzheimer's disease patients (van Rooden et al., 2009) and in vivo imaging of healthy volunteers (Duyn et al., 2007) we developed a scoring method to capture the appearance of the cortex on SW images. We defined a normal cortex based on the following criteria: a) a cortical ribbon containing one homogeneous layer with a higher signal intensity as compared to the adjacent white matter (WM), b) a cortical ribbon containing two well-defined, homogeneous layers, with the superficial layer demonstrating a higher signal intensity compared to the deepest layer (the layer adjacent to the WM) and the WM, or c) a cortical ribbon with three layers: the same layers as previously described separated by a third thin layer with a lower signal intensity than the other two layers (fig. 1). Abnormal cortex was classified as a deviation from the normal patterns described above, showing the presence of well-defined foci of signal loss (hypointense foci) and/or more diffuse areas with lower signal intensity in the superficial layer as compared to the adjacent WM (a diffuse band) (fig. 1). Features were scored as present or absent per subject in several predefined gyri of the frontal lobe (table 1). Uniform window settings were used for all images. Images were scored by two neuroradiologists (B.E. and M.L.) who were blinded for the diagnosis in a consensus reading.

Statistics

A Mann-Whitney U-test was used to assess differences in age and MMSE, and a chi-square test was used to assess differences in gender between Alzheimer's disease and control groups. For each feature (hypointense foci and/or a diffuse band), a Fisher's exact test was performed per brain region. Positive and negative predictive values of the features to detect Alzheimer's disease were calculated per brain region. All statistical analyses were performed with the Statistical Package of Social Sciences (SPSS 17.0.1; SPSS, Chicago, Ill).

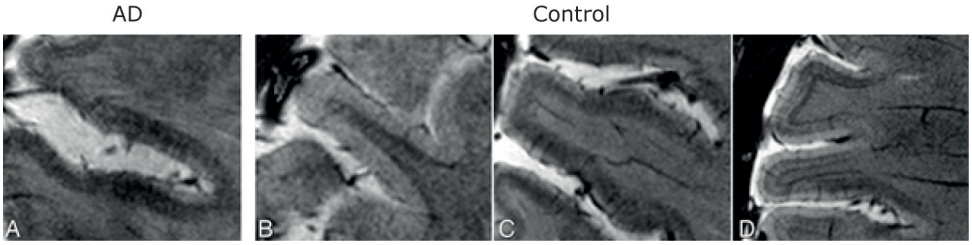

Figure 1: The observed variations of in vivo 7T SW imaging appearance of the human cortex Shown are the middle/inferior frontal brain area of an Alzheimer's disease patient (A) and healthy elderly controls (B, C, D). An clear example of a cortical ribbon containing a hypointense diffuse band is observed in the Alzheimer's disease patient (A). Please note the blurring of the edges of the layers. (B) shows an example of a cortical ribbon containing one regular layer with higher signal intensity than the adjacent WM. In (C) a cortical ribbon is shown containing two well-defined layers. (D) shows a cortical ribbon containing three well-defined layers.

B. Post-mortem MRI study:

Study design

To investigate the histological substrates responsible for the observed in vivo MRI changes at 7T, we applied similar scan methods on postmortem material of Alzheimer's disease patients and controls using a vertical-bore 9.4 T system (Bruker Biospin, Ettlingen, Germany). For each sample high-resolution (isotropic 40 μm voxels) images were acquired, as well as images with a similar resolution (isotropic 200 μm voxels) as were used in the in vivo study. The lower resolution MR images were acquired to help the translation between the in vivo and ex vivo MR data sets. The high-resolution MR images helped to identify the particular MR images that matched best with the 8-μm thick histological sections.

Sample preparation

Brain tissue was obtained from the tissue bank of the Department of Pathology at our institution and from the Netherlands Brain Bank (NBB, Netherlands Institute for Neuroscience, Amsterdam). Following a post-mortem interval of <19 hours, brains were resected and stored in 4% paraformaldehyde. At both institutions brain tissue was examined histologically for the presence of Alzheimer's disease-related pathology and scored using the Braak classification (Braak et al., 2006). Based on availability 6 samples with a clinical diagnosis of Alzheimer's disease by histological confirmation were selected, as well as 3 age-matched non-demented controls (table 2). Patient anonymity was strictly maintained. All tissue samples were handled in a coded fashion, according to Dutch national ethical

guidelines (Code for Proper Secondary Use of Human Tissue, Dutch Federation of Medical Scientific Societies). To avoid formalin-induced artifacts in the MR images only material fixed for a period of between 3 months and 2 years was used (van Duijn et al., 2011). From each subject 1 tissue block of approximately 4 x 15 x 15 mm3 was resected from the medial temporal lobe using a vibratome (VT1000S, Leica, Germany). Care was taken to ensure that the samples were resected with a similar gyral orientation. Residual formalin was washed out by placing the samples in phosphate buffered saline (PBS) for >24 hours to partially restore MR relaxation parameters (Shepherd et al., 2009). For MRI, each sample was placed in a customized tissue container and immersed in a proton-free fluid (Fomblin LC08, Solvay). Air was removed by application of a vacuum for several minutes (van Duijn et al., 2011).

Post-mortem MRI

Scans were acquired on a 9.4 Tesla vertical bore MRI system, equipped with a 1 T/m actively-shielded gradient insert and Paravision 5.0 imaging software (Bruker Biospin, Ettlingen, Germany). A 20-mm diameter bird-

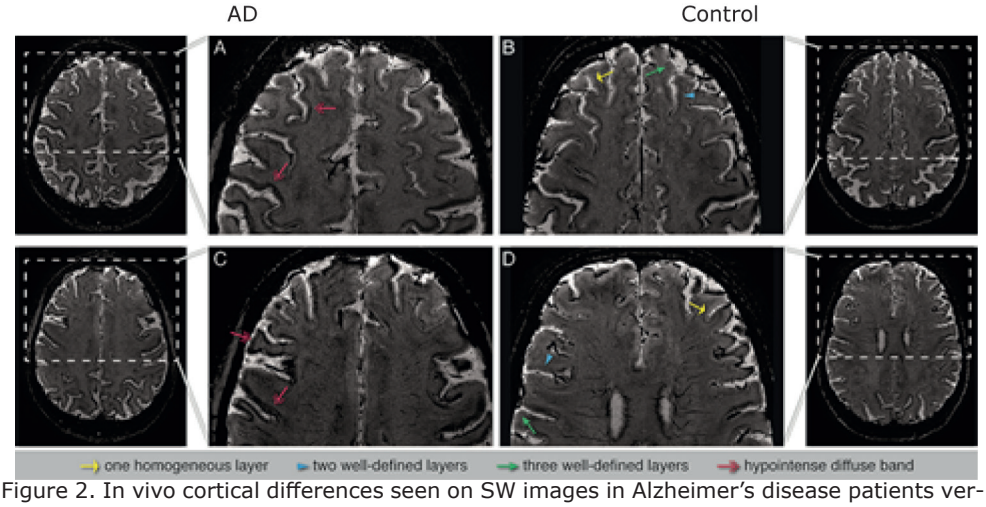

Figure 2. In vivo cortical differences seen on SW images in Alzheimer's disease patients versus age-matched control subjects Regional distribution of the observed variations of in vivo 7T SW imaging appearance as presented in fig. 1, shown in an Alzheimer's disease patient and a control subject. The left two columns (A and C) show an Alzheimer's disease patient and the right two columns (B and D) a control subject. The upper row (A and B) shows the superior frontal region, the lower row (C and D) the middle and inferior frontal region. In the Alzheimer's disease patient a diffuse band is seen in both regions of the frontal lobe and the double arrows show several locations containing this band whereas in the control subject this diffuse band is absent and a regular layer (arrow), two-well defined layers (arrowhead) and three-well defined layers (small arrow) could be detected.

cage transmit/receive coil was used to acquire T2*-weighted 3D gradient echo images with TR = 75 ms; TE = 22.5 ms; flip angle = 25° at either 200 µm isotropic resolution with 20 signal averages, or 40 µm isotropic resolution with 28 signal averages. The average scan time per resolution was approximately 40 minutes (200 µm resolution) or 25 hours (40 µm resolution), with minor differences between samples of slightly different sizes. To create SW images comparable to in vivo scans, the 200 µm resolution phase images were unwrapped using a k-space Hanning filter with a width set to 50% of the image size (Wang et al., 2000). Final SW images were reconstructed from the original images by four phase mask multiplications (Haacke et al., 2004). All data processing was performed with MatLab (MathWorks, Natick, MA).

Postmortem image analysis

For assessment of ex vivo SW images we used the same criteria as were used in vivo for defining normal and abnormal cortex (hypointense bands and hypointense foci). In addition, since the ex vivo images showed increased anatomical detail compared to the in vivo scans (due to the absence of physiological motion), a third category of abnormal cortex could be added, namely diffuse areas with low signal intensity, not extending parallel to the cortical surface (as in healthy tissue) but instead expanding locally in an irregular fashion throughout the cortex, a feature which we have termed "clouds". Window settings were optimized for each sample based on the WM and gray matter (GM) histogram. The 200 µm SW images were scored blinded for diagnosis by a neuroradiologist (M.v.B) and MR-microscopy expert (L.v.d.W) in a consensus reading.

Histology and electron microscopy

All brain samples were paraffin-embedded and serially cut into 8-µm thick sections. Tissue morphology was assessed by standard hematoxylin-eosin (HE) staining. Iron was detected using a 3'3-diaminobenzidine-tetrahydrochloride (DAB) enhanced Perls' staining protocol for light microscopy and EM which has shown to be the most sensitive to detect iron-positive structures in paraffin-embedded human AD brain tissue (Meguro et al., 2007; van Duijn et al., 2013). Consecutive sections were (co-)stained for amyloid-beta (Aβ), paired helical filament-tau (AT8), myelin (protolipid-protein (PLP)), microglia (CD68 and HLA-DR) and activated astrocytes (GFAP) (Supplementary table 1). Endogenous peroxidase was blocked by 30 minutes of incubation in methanol with 0.02% H2O2. After these

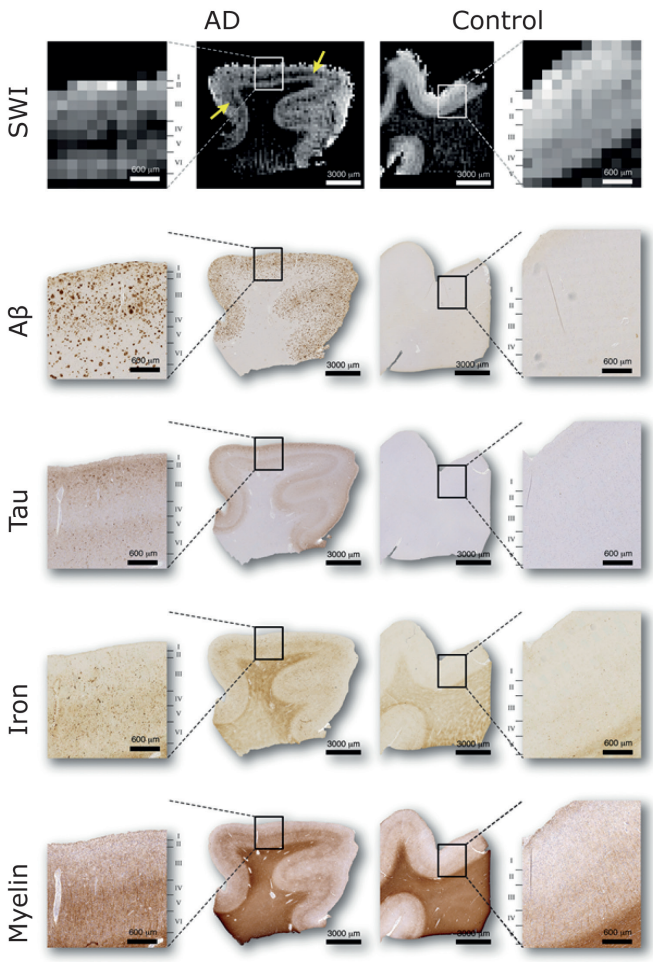

Figure 3. Comparison of post-mortem SW images with histology The SW image of the Alzheimer's disease patient (table 2 subject 7) showed a midcortical hypointense band (yellow arrows) in addition to several focal hypointensities, as opposed to a clear homogeneous cortex as seen in the control subject (table 2 subject 1). For detailed evaluation similar regions of interest of the cortex are shown alongside each corresponding main image and the cortical layers have been assigned accordingly. Neither the cortical distribution of Aβ or tau matched the hypointense band. Tau typically showed a band-like pattern in cortical layers II – III and V, and so is not co-localized in the layer corresponding to MR signal decrease. Both iron and myelin correlated with the observed pattern of band-like hypointensities, including a diminished staining in the inner cortical layers V and VI. As compared to the control, the iron staining of the Alzheimer's disease subject showed an increase in cellular deposits and diffuse iron within the neuropil, mainly centred around cortical layer IV spreading to both sides with overlap in layers III and IV. The myelin distribution visualized by the PLP-immunostaining showed a similar pattern of increased staining in the Alzheimer's disease subject resulting from a denser network of thin myelinated fibres. Similar to previous reports, in the Alzheimer's disease patient the cortex also contained several small roundish areas devoid of myelinated fibres suggesting the presence of amyloid plaques based on their morphological appearance (Mitew et al., 2010.)

pre-treatments, non-specific binding was minimized by incubation with 10% fetal calf serum (DakoCytomation). Labelling was visualized by DAB staining (DakoCytomation). All sections were digitized with a microscope scanner (Panoramic, 3DHistotech, Hungary) for global and microscopic evaluation. To assess co-localization of cellular iron with CD68, HLA-DR or GFAP-positive cells, sections stained for iron as described above were subsequently treated according to the previously described immunohistochemical procedures except for using an Alexa647-labeled secondary

anti-mouse antibody for immunofluorescence. Co-localization of these antigens with iron was assessed using a confocal fluorescence microscope (LSM 510, Zeiss, Germany). Iron-stained ultrathin (100 nm) sections were examined by electron microscopy (JEM-1011, JEOL, Germany) to assess the exact localization of the cortical iron in the neuropil.

Histology-MRI correlation

The digitized histological sections were matched with their corresponding high-resolution (40 µm) MR images by visual comparison of the contour and vascular architecture of each section. The corresponding low-resolution SW image that matched best with the histological section could then be identified directly since the two SW image datasets are inherently co-registered. To assess the histological substrate of the cortical changes observed on MR images, the digitized histological sections were first inspected at low magnification (2x) alongside the corresponding low-resolution SW image. Subsequently, these areas were further analyzed microscopically at higher magnification (40x) to look for the microscopic changes underlying the MR. All observations were independently verified by three neuropathologists (R.N., S.v.D., M.F.).

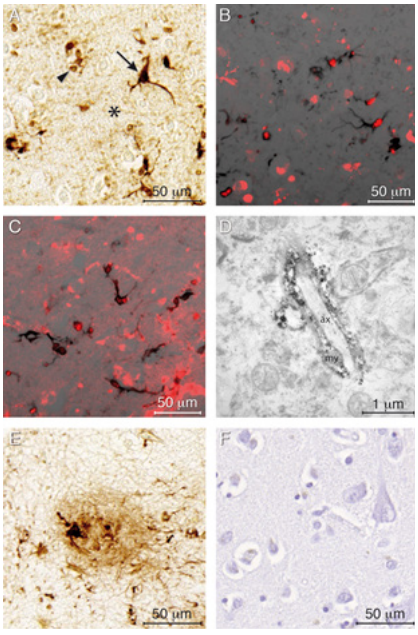

Figure 4. Characterization of intracortical iron distribution in Alzheimer's disease brain tissue Shown are the different types of cellular and neuropilar intracortical iron in the medial temporal lobe of an Alzheimer's disease patient (table 2 subject 7). (A) Indicated by the brown colour due to the modified 3'3-DAB enhanced Perls' iron staining, iron is present as perinuclear (arrow head) and stellate cellular deposits (arrow), and as diffuse iron spread throughout the neuropil (asterix). Morphologically the cellular iron was attributed to oligodendrocyte or microglia cells. The latter was further verified by the co-localization of iron (black) with (B) CD68 (red) and (C) HLA-DR (red) immunostaining. As indicated by both stainings, even in close proximity to these iron-bearing microglia, several microglia were present that were completely devoid of iron. (D) Ultrastructurally, as shown by EM, neuropil iron was found to be located in the myelin sheets folded around an axon. (E) A example of iron found associated with an amyloid plaque. (F) The negative iron staining of a consecutive section did not result in any DAB enhancement, thereby confirming specificity of the iron stain (axon, ax; myelin sheet, my)

Results

The characteristics of the participants for in vivo MRI are shown in table 1. No difference in age ($p = 0.497$) or gender ($p = 0.893$) was found between patient and control groups. Scores for global cognitive functioning (MMSE score) were significantly higher in controls (29.2 points; range 27-30) than in patients with Alzheimer's disease (22.5 points, range 19-26), $p<0.001$. 7T SW images of the frontal lobe of probable Alzheimer's disease patients (n=14) were visually compared to those of control subjects (n=15).

We developed a scoring method to rate the cortical appearance based on previous 7T observations in normal brain and postmortem observations in Alzheimer's disease patients, distinguishing normal-appearing cortical patterns with one or more homogeneous layers from hypointense foci or hypointense diffuse bands (fig. 1). Clear in vivo differences between Alzheimer's disease patients and controls were seen in terms of the presence of diffuse hypointense bands on the SW images (table 1, fig. 2). Within the frontal lobe, these patterns were found in the middle and inferior frontal gyri in eight out of 14 patients, whereas these diffuse bands were not observed in any of the control subjects. In these frontal gyri, the diffuse hypointense band was significantly more prevalent in Alzheimer's disease patients as compared to controls ($p = 0.001$), with positive predictive and negative values of 100% and 71%, respectively. In the superior frontal gyrus, a similar hypointense band was observed in only two out of the 14 Alzheimer's disease patients and in none of the control subjects: there was no significant difference between the two groups ($p = 0.224$). For this specific cortical region, corresponding positive and negative predictive values were 100% and 55%, respectively. Foci of signal loss were not observed in the frontal lobe in either Alzheimer's disease patients or control subjects.

Post-mortem cerebral cortex samples of six Alzheimer's disease cases and three age-matched controls were scanned with a similar SWI protocol as for the in vivo MRI. Two of the controls showed a normal cortex. The control subject with an abnormal cortex revealed Alzheimer's disease-type pathology (Braak stage III), despite the absence of an ante-mortem clinical Alzheimer's disease diagnosis. We therefore discuss the findings in this case separately.

In all postmortem AD samples (6 out of 6), an abnormal cortex was observed on SW images (table 2). Hypointense bands were observed in five out of six AD cases, and in the control with Braak III. Due to the lack of

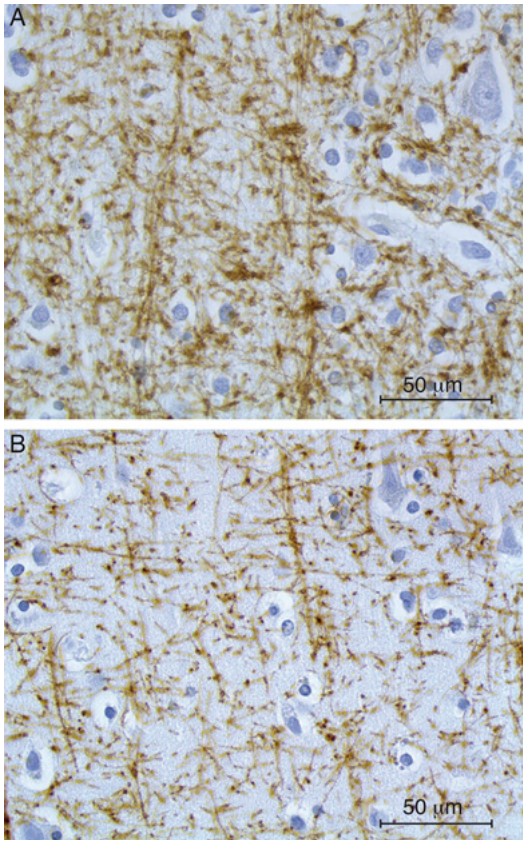

Figure 5. Structural alterations of intracortical myelin
In addition to the observed differences in myelin highlighted by fig. 3, this figure presents a more detailed comparison of the intracortical myelin of the medial temporal lobe of (A) an Alzheimer's disease patient (table 2 subject 4) and (B) a non-demented age-matched control (table 2 subject 1). Shown are midcortical regions (layer IV) with a comparable orientation assessed by a PLP-immunostaining (brown). At this higher magnification, the intracortical myelin in the Alzheimer's disease subjects was characterized by an accentuated PLP staining due to changes in myelin structure comprising fragmentation, increased segmental tortuosity and bead-like varicosities. As a result the PLP staining of the Alzheimer's disease cortex appeared disorganized with loss of individually discernable fibres and orientation when compared to the cortex of the control subjects.

physiological movements, the ex vivo images that were acquired with a similar resolution as the in vivo images provided more anatomical detail, and demonstrated that the hypointense bands did not cover the full width of the cortex, but were located centrally in the cortex (fig. 3). Hypointense foci were observed in 2 out of 6 AD cases, and in the 1 control specimen with Braak III. In addition to the scoring criteria defined for the in vivo scans, in these post-mortem samples a third category of cortical disturbance could be observed, consisting of cloud-like areas of low signal intensity with less alignment along, and more expansion through, the cortical layers (4 out of 6 AD cases, and in the control subject with Braak III). Comparing radiological and histological data of the same sample, the epicentre of the hypointense bands and clouds observed on the ex vivo MR images could be localized in cortical layer IV. Subsequently, we assessed which of the histological markers (Aβ, tau, iron, and myelin) showed a similar distribution over the cortical layers to the hypointense bands and clouds. We observed that the hypointense bands and clouds on MRI co-lo-

calized with areas characterized by an increased presence of iron and changes in myelin structure (fig. 3). Only cortices that were scored as abnormal on SW images demonstrated these accentuated local patterns for iron and myelin on histological examination. Interestingly, no co-localization was observed between the hypointense bands and clouds on MRI and areas staining for Aβ or tau. Tau pathology typically affected cortical layers II – III and V. Aβ staining was present to an equal extent across all cortical layers. Microscopically, some of the hypointense foci observed on the ex vivo images corresponded to large amyloid plaques, but these focal signal voids barely contributed to the observed hypointense cortical bands.

Since the pattern of the abnormalities observed on MRI corresponded best with the patterns observed on iron and myelin-stained tissue, we examined these stainings in more detail. Microscopically, using higher magnification, four different types of iron accumulation were observed in the cortex: 1) diffuse neuropil deposition associated with myelinated fibres, 2) dense stellate cytoplasmic iron accumulation in microglial cells, 3) a dense thin line of perinuclear iron accumulation in oligodendroglial and microglial cells, and 4) iron associated with amyloid plaques (fig. 4). All 4 types of iron deposits were more abundant in the subjects with an abnormally appearing cortex on postmortem MRI, including the control subject with Braak III. The first 3 types of iron deposits were localized differently in the cortical layers: neuropil iron accumulation was centered in layer IV, extending into layers III and V of the cortex; stellate glial aggregates were most abundant in the middle cortical layers (layers III and IV), but were also present to a lesser extent in the deep cortical layers (layers V and VI), and perinuclear glial iron accumulation was most abundant in layers V and VI, followed by layers IV and III (fig. 3). In addition, increased microglial and neuropil iron accumulations were also observed in areas characterized by cloud-like hypointensities on MRI. EM analysis revealed that the diffuse iron in the neuropil was located predominantly in oligodendrocytic myelin sheaths (fig. 4D).

The association of iron with myelin sheaths in the neuropil led us to examine the cortical myelin in more detail using a PLP staining. Interestingly, the intensity of myelin staining also showed a colocalization with the low signal intensity bands and clouds on MRI (fig. 3). Histologically, these areas were characterized by an accentuated PLP staining due to changes in myelin structure comprising fragmentation, increased segmental tortuosity and bead-like varicosities, centralized in layer IV, but extending to

layers III and V in the AD patients (fig. 3 and 5). Furthermore, as expected, small round plaque-like areas that were devoid of any myelin fibres were observed in cortical areas containing a high number of Aβ deposits.

Discussion

Using 7T MRI we observed striking differences in vivo in the frontal cortex between AD patients and age-matched controls. In patients with probable AD we found a disturbance of the layered structure of the cortex. Previous studies in healthy subjects demonstrated that cortical lamination at 7T reflects intracortical myeloarchitecture (Duyn et al., 2007; Fukunaga et al., 2010; Cohen-Adad et al., 2012), and this normal pattern of cortical lamination was attributed to differences in myelin-associated iron and myelin lipids in the different cortical layers (Duyn et al., 2007). Our current study shows that in AD patients the cortical areas of altered SW contrast co-localize with areas of increased microglia- and myelin-associated iron accumulation and also with changes in myelin cytoarchitecture. However, our data also demonstrate that the pattern of the changes observed on MRI does not correspond to the pattern of amyloid deposits. These observations are not in line with the previous assumption, mostly based on animal experiments, that T2*-weighted and SW imaging contrast in Alzheimer's disease primarily reflects the presence of iron associated with amyloid plaques (Duyn et al., 2007; van Rooden et al., 2009; Meadowcroft et al., 2009; Chamberlain et al., 2011). Our observations of disturbed iron accumulation and myelin architecture have important implications for in vivo diagnosis of AD, and also for the understanding of the pathophysiological mechanisms underlying this disease.

According to the amyloid hypothesis oligomeric forms of Aβ are the trigger for a cascade of events that ultimately results in dementia. However, there is increasing evidence that a range of other ethological factors have an important impact on this cascade, presumably by interacting with the Aβ aggregates or by subsequent cellular changes which follow it (Herrup, 2010; Bartzokis, 2011; Fjell and Walhovd, 2012). In our study, we found a close correlation between SW MRI contrast changes, myelin changes and increased iron accumulation in cortices with Alzheimer's disease pathology. Interestingly, changes in iron metabolism and myelin breakdown have both been mentioned as potential upstream mechanisms for Alzheimer's disease (Herrup, 2010; Bartzokis, 2011).

Iron and myelin are closely associated in the brain. Seventy percent of the brain's iron is located in oligodendrocytes. Maturation of oligodendro-

cytes and myelin synthesis are both dependent on the availability of iron (Todorich et al., 2009; Bartzokis, 2011). During demyelination processes in disease, as well as during normal myelin turnover, iron is assumed to be released from myelin into the brain tissue (Bartzokis, 2011), Our observation of increased iron in microglial cells (which have an important phagocytic role) in areas of altered myelin structure suggests that the observed MRI changes are a reflection of increased demyelination.

Cortical demyelination has been observed previously in AD, but mainly as areas of focal myelin loss in the immediate vicinity of amyloid plaques (Mitew et al., 2010; Serrano-Pozo et al., 2010). We also observed this pattern of myelin loss in our samples, but it was much less prominent than the more diffuse changes in myelin structure (increased fragmentation, tortuosity, and bead-like varicosities) which we report here. To our knowledge, these findings have not been reported before in human Alzheimer's disease, but strikingly similar myelin alterations were recently discovered in a mouse model of Alzheimer's disease (Chen et al., 2011).

Apart from its role in myelin metabolism, iron is an important upstream and downstream modulator of several molecular pathways in Alzheimer's disease. Recently it was demonstrated that APP plays a physiological role in preventing iron-mediated oxidative stress in the brain (Duce et al., 2010). In Alzheimer's disease, zinc accumulation in amyloid plaques and loss of soluble tau interfere with APP's ferroxidase activity, causing increased neuronal iron accumulation. Furthermore, there is evidence that APP processing through the amyloidogenic and non-amyloidogenic pathways is affected by iron (Duce et al., 2010; Lei et al., 2012). Finally, experimental data have demonstrated that iron may accelerate Aβ oligomerization (Roberts et al., 2012). Based on these observations, it has been suggested that iron could be an important biomarker of AD (Collingwood and Dobson 2006; Zhu et al., 2009).

The data presented here show convincing evidence that the cortical myelin cytoarchitecture and iron distribution are disturbed in Alzheimer's disease patients. Although these changes might not be central to the pathogenesis of Alzheimer's disease, the ability to visualize them by MRI creates a putative novel biomarker with the potential to reflect an as yet under-appreciated change that may accompany the progression of Alzheimer's disease. However, our data are preliminary since they have been generated in a limited number of patients and healthy controls, and cover only a limited part of the brain. Postmortem, we observed these changes in SWI contrast in all patients with confirmed Alzheimer's dis-

ease. In vivo, we observed these changes in cortical appearance only in a sub-set of patients; one reason for this discrepancy may be that the patients have been included based on a clinical diagnosis (NINCDS-ADRDA criteria), which is known to have a limited diagnostic accuracy (77 - 85%) (Jobst et al., 1998). Further studies, comprising larger patient series and additional controls populations of patients with different types of dementia are required to assess the potential of the cortical changes we observed to constitute true diagnostic biomarkers for AD. There are many other important and related questions, such as whether the presence of cortical changes is associated with reduced cognitive function, whether the changes appear early in the course of AD, and whether the frontal lobes are the best regions in which to detect these early changes. Additional in vivo and postmortem research on the correlation between ultra-high field MRI and pathology will allow us to further elucidate the role of iron and myelin in the pathogenesis of Alzheimer's disease. Overall, the analysis of the cortical changes via visual inspection and simple scoring criteria, without the need for quantitative measurements or sophisticated image processing techniques, makes the proposed method very attractive as a diagnostic and research tool in a clinical setting.

Acknowledgements
The authors thank Ingrid Hegeman-Kleinn for technical assistance. This research was performed within the framework of CTMM, the Centre for Translational Molecular Medicine (www.ctmm.nl), project LeARN (grant 02N-101).

Reference List

Alves L, Correia AS, Miguel R, Alegria P, Bugalho P. Alzheimer's disease: a clinical practice-oriented review. Front Neurol 2012; 3: 63.

Bartzokis G. Alzheimer's disease as homeostatic responses to age-related myelin breakdown. Neurobiol Aging 2011; 32: 1341-71.

Braak H, Alafuzoff I, Arzberger T, Kretzschmar H, Del TK. Staging of Alzheimer disease-associated neurofibrillary pathology using paraffin sections and immunocytochemistry. Acta Neuropathol 2006; 112: 389-404.

Chamberlain R, Wengenack TM, Poduslo JF, Garwood M, Jack CR, Jr. Magnetic resonance imaging of amyloid plaques in transgenic mouse models of Alzheimer's disease. Curr Med Imaging Rev 2011; 7: 3-7.

Chen H, Epelbaum S, Delatour B. Fiber Tracts Anomalies in APPxPS1 Transgenic Mice Modeling Alzheimer's Disease. J Aging Res 2011; 2011: 281274.

Cohen-Adad J, Polimeni JR, Helmer KG, Benner T, McNab JA, Wald LL et al. T(2)* mapping and B(0) orientation-dependence at 7 T reveal cyto- and myeloarchitecture organization of the human cortex. Neuroimage 2012; 60: 1006-14.

Collingwood J, Dobson J. Mapping and characterization of iron compounds in Alzheimer's tissue. J Alzheimers Dis 2006; 10: 215-22.

Duce JA, Tsatsanis A, Cater MA, James SA, Robb E, Wikhe K et al. Iron-export ferroxidase activity of beta-amyloid precursor protein is inhibited by zinc in Alzheimer's disease. Cell 2010; 142: 857-67.

Duyckaerts C, Delatour B, Potier MC. Classification and basic pathology of Alzheimer disease. Acta Neuropathol 2009; 118: 5-36.

Duyn JH, van Gelderen P, Li TQ, de Zwart JA, Koretsky AP, Fukunaga M. High-field MRI of brain cortical substructure based on signal phase. Proc Natl Acad Sci U S A 2007; 104: 11796-801.

Fjell AM, Walhovd KB. Neuroimaging results impose new views on Alzheimer's disease--the role of amyloid revised. Mol Neurobiol 2012; 45: 153-72.

Fukunaga M, Li TQ, van Gelderen P, de Zwart JA, Shmueli K, Yao B et al. Layer-specific variation of iron content in cerebral cortex as a source of MRI contrast. Proc Natl Acad Sci U S A 2010; 107: 3834-9.

Haacke EM, Xu Y, Cheng YC, Reichenbach JR. Susceptibility weighted imaging (SWI). Magn Reson Med 2004; 52: 612-8.

Herrup K. Reimagining Alzheimer's disease--an age-based hypothesis. J Neurosci 2010; 30: 16755-62.

Jack CR, Jr., Knopman DS, Jagust WJ, Shaw LM, Aisen PS, Weiner MW et al. Hypothetical model of dynamic biomarkers of the Alzheimer's pathological cascade. Lancet Neurol 2010; 9: 119-28.

Jobst KA, Barnetson LP, Shepstone BJ. Accurate prediction of histologically confirmed Alzheimer's disease and the differential diagnosis of dementia: the use of NINCDS-ADRDA and DSM-III-R criteria, SPECT, X-ray CT, and Apo E4 in medial temporal lobe dementias. Oxford Project to Investigate Memory and Aging. Int Psychogeriatr 1998; 10: 271-302.

Karran E, Mercken M, De Strooper B. The amyloid cascade hypothesis for Alzheimer's disease: an appraisal for the development of therapeutics. Nat Rev Drug Discov 2011; 10: 698-712.

Langbaum JB, Chen K, Lee W, Reschke C, Bandy D, Fleisher AS et al. Categorical and correlational analyses of baseline fluorodeoxyglucose positron emission tomography images from the Alzheimer's Disease Neuroimaging Initiative (ADNI). Neuroimage 2009; 45: 1107-16.

Lei P, Ayton S, Finkelstein DI, Spoerri L, Ciccotosto GD, Wright DK et al. Tau deficiency induces parkinsonism with dementia by impairing APP-mediated iron export. Nat Med 2012; 18: 291-5.

McKhann G, Drachman D, Folstein M, Katzman R, Price D, Stadlan EM. Clinical diagnosis of Alzheimer's disease: report of the NINCDS-ADRDA Work Group under the auspices of Department of Health and Human Ser-

vices Task Force on Alzheimer's Disease. Neurology 1984; 34: 939-44.

Meadowcroft MD, Connor JR, Smith MB, Yang QX. MRI and histological analysis of beta-amyloid plaques in both human Alzheimer's disease and APP/PS1 transgenic mice. J Magn Reson Imaging 2009; 29: 997-1007.

Meguro R, Asano Y, Odagiri S, Li C, Iwatsuki H, Shoumura K. Nonheme-iron histochemistry for light and electron microscopy: a historical, theoretical and technical review. Arch Histol Cytol 2007; 70: 1-19.

Mitew S, Kirkcaldie MT, Halliday GM, Shepherd CE, Vickers JC, Dickson TC. Focal demyelination in Alzheimer's disease and transgenic mouse models. Acta Neuropathol 2010; 119: 567-77.

Montine TJ, Phelps CH, Beach TG, Bigio EH, Cairns NJ, Dickson DW et al. National Institute on Aging-Alzheimer's Association guidelines for the neuropathologic assessment of Alzheimer's disease: a practical approach. Acta Neuropathol 2012; 123: 1-11.

Natte R, Maat-Schieman ML, Haan J, Bornebroek M, Roos RA, van Duinen SG. Dementia in hereditary cerebral haemorrhage with amyloidosis-Dutch type is associated with cerebral amyloid angiopathy but is independent of plaques and neurofibrillary tangles. Ann Neurol 2001; 50: 765-72.

Roberts BR, Ryan TM, Bush AI, Masters CL, Duce JA. The role of metallobiology and amyloid-beta peptides in Alzheimer's disease. J Neurochem 2012; 120 Suppl 1: 149-66.

Rombouts SA, Barkhof F, Goekoop R, Stam CJ, Scheltens P. Altered resting state networks in mild cognitive impairment and mild Alzheimer's disease: an fMRI study. Hum Brain Mapp 2005; 26: 231-9.

Rowe CC, Villemagne VL. Brain Amyloid Imaging. J Nucl Med 2011.
Schar M, Kozerke S, Fischer SE, Boesiger P. Cardiac SSFP imaging at 3 Tesla. Magn Reson Med 2004; 51: 799-806.

Serrano-Pozo A, William CM, Ferrer I, Uro-Coste E, Delisle MB, Maurage CA et al. Beneficial effect of human anti-amyloid-beta active immunization on neurite morphology and tau pathology. Brain 2010; 133: 1312-27.

Shepherd TM, Thelwall PE, Stanisz GJ, Blackband SJ. Aldehyde fixative solutions alter the water relaxation and diffusion properties of nervous tissue. Magn Reson Med 2009; 62: 26-34.

Todorich B, Pasquini JM, Garcia CI, Paez PM, Connor JR. Oligodendrocytes and myelination: the role of iron. Glia 2009; 57: 467-78.

van Duijn S, Nabuurs RJ, van Duinen SG, Natte R. Comparison of histological techniques to visualize iron in paraffin-embedded brain tissue of patients with Alzheimer's disease. J Histochem Cytochem 2013; 61: 785-92.

van Duijn S, Nabuurs RJ, van Rooden S, Maat-Schieman ML, van Duinen SG, van Buchem MA et al. MRI artifacts in human brain tissue after prolonged formalin storage. Magn Reson Med 2011; 65: 1750-1758.

van Rooden S, Maat-Schieman ML, Nabuurs RJ, van der Weerd L, van DS, van Duinen SG et al. Cerebral amyloidosis: postmortem detection with human 7.0-T MR imaging system. Radiology 2009; 253: 788-96.

Versluis MJ, Peeters JM, van Rooden S, van der Grond J, van Buchem MA, Webb AG et al. Origin and reduction of motion and f0 artifacts in high resolution T2*-weighted magnetic resonance imaging: application in Alzheimer's disease patients. Neuroimage 2010; 51: 1082-8.

Wang Y, Yu Y, Li D, Bae KT, Brown JJ, Lin W et al. Artery and vein separation using susceptibility-dependent phase in contrast-enhanced MRA. J Magn Reson Imaging 2000; 12: 661-70.

Zhu WZ, Zhong WD, Wang W, Zhan CJ, Wang CY, Qi JP et al. Quantitative MR phase-corrected imaging to investigate increased brain iron deposition of patients with Alzheimer disease. Radiology 2009; 253: 497-504.